ORIGINAL PAPER

High-Field EPR Investigation and Detailed Modeling of the Magnetoanisotropy Tensor of an Unusual Mixed-Valent $Mn_2^{IV}Mn_2^{III}Mn^{II}$ Cluster

Xiaoling Wang[1,2] · Ashlyn R. Hale[2,3] · Stephen Hill[1,2,4] ·
George Christou[2,3]

© The Author(s), under exclusive licence to Springer-Verlag GmbH Austria, part of Springer Nature 2022

Abstract

Multifrequency (128 and 256 GHz) high-field electron paramagnetic resonance measurements up to 14.5 T over the temperature range 8.0 to 30.0 K were performed on powder samples of a recently reported salt of the cluster cation $[Mn_5O_4(phth)_3(phthH)(bpy)_4]^+$ (**1**; $Mn_2^{IV}Mn_2^{III}Mn^{II}$). Spectral simulations were performed to quantify the zero-field splitting parameters of **1**, further supporting the previously assigned $S = \frac{7}{2}$ ground state. **1** possesses a highly biaxial zero-field splitting tensor ($E/D = 0.227$) with overall easy-plane anisotropy ($D > 0$) arising from the near-perpendicular angle between the Jahn–Teller axes of the two Mn^{III} that contribute a majority of the magnetic anisotropy. A microscopic model has been developed that relates the sign of D and the degree of ortho-rhombicity, E/D, to the angle between the two Jahn–Teller axes. The additional fine structure and peak-splitting features not represented by the simulations were attributed to population of excited states or the weak intermolecular interactions previously observed in the crystal structure.

1 Introduction

Manganese is a versatile element with rich redox chemistry essential to both life on Earth and our modern society. It is a common component in numerous biological, environmental, and industrial systems, often as a catalyst, an additive, or

✉ Stephen Hill
  shill@magnet.fsu.edu

1   National High Magnetic Field Laboratory, Tallahassee, FL 32310, USA

2   Center for Molecular Magnetic Quantum Materials, Gainesville, FL 32611, USA

3   Department of Chemistry, University of Florida, Gainesville, FL 32611, USA

4   Department of Physics, Florida State University, Tallahassee, FL 32306, USA

similar. For example, by far the greatest industrial use of Mn is as an additive to harden steel [1, 2] while, in the environmental arena, Mn oxides are employed for groundwater remediation from harmful pollutants, such as heavy metals, organic dyes, and other organic contaminants [1, 3]. Respiring life depends on O_2 gas production from the water oxidation reaction catalyzed by the photosynthetic oxygen-evolving complex (OEC) in green plants and cyanobacteria, which is a Mn_4CaO_5 unit comprising a $\{Mn_3CaO_4\}$ distorted-cubane bridged by oxide ions to a fourth, external Mn ion [4–10]. Efficient synthetic water splitting systems based on Earth-abundant 3d metals are promising candidates to address climate change concerns by providing viable routes to hydrogen fuel production [11–14]. The latter is inspiring research in Mn/O cluster chemistry, resulting in OEC model compounds comprising the $[Mn_3^{IV}CaO_4]^{6+}$ cubane by itself [15, 16] or bound to an external Ca^{2+} [17] or Mn^{3+} [18], as well as other related molecular clusters [19–31]. Most recently, $[Mn_{12}O_{12}(O_2CC_6H_3(OH)_2)_{16}(H_2O)_4]$, possessing a central $Mn_4^{IV}O_4$ cubane, has been shown to be soluble, stable in water, and to function as an efficient electro-catalyst for water oxidation with a low over-potential of ~ 334 mV at pH 6 [32].

Electron paramagnetic resonance (EPR) spectroscopy is a powerful tool in molecular Mn-oxo chemistry, particularly at high magnetic fields [33, 34], allowing the accurate determination of spin Hamiltonian parameters, such as ground-state spin (S), electron g-tensor, and zero-field splitting (ZFS) parameters in magnetic molecules [35–38], including single-molecule magnets (SMMs) [39–44]. It has also proven a powerful means to study atomic clock transitions in mononuclear Ho^{III} and Lu^{II} complexes for molecular spin qubit applications [45, 46] and has served as a crucial characterization technique in structural biology [47–50].

EPR has been of particular benefit to the study of the different oxidation states, $\mathbb{S}_n$ ($n=0–4$), occurring in the four-electron catalytic cycle, the so-called Kok cycle, of the OEC in photosynthesis. Each $\mathbb{S}_n$ state exhibits diagnostic EPR signatures, and often multiple EPR signatures depending on the differing conditions under which it is generated, so the availability of the sensitive EPR probe is invaluable. For example, the OEC $\mathbb{S}_0$ state is at the $Mn_3^{III}Mn^{IV}$ oxidation level and exhibits a small ground-state spin of $S=\frac{1}{2}$ [51]. A recent EPR analysis has established two forms of the $\mathbb{S}_1$ ($Mn_2^{IV}Mn_2^{III}$) state [52] due to Jahn–Teller (JT) isomerism, i.e., differing orientations of Mn^{III} JT axes, a phenomenon originally identified in the $[Mn_{12}O_{12}(O_2CR)_{16}]$ $(H_2O)_4]$ SMM family [53–55]. The two $\mathbb{S}_1$ forms give different EPR signals: one is $S=1$ with an EPR signal at $g=4.8$, and the other is $S=3$ and exhibits a $g=12$ signal [52]. Similarly, the $\mathbb{S}_2$ ($Mn^{II}Mn_3^{IV}$) state displays two EPR signals depending on generation conditions, an $S=\frac{1}{2}$ state with a $g \sim 2$ signal, and an $S \geq \frac{5}{2}$ state with $g \geq 4.1$ [56–60]. Likewise, the water-unbound $\mathbb{S}_3$ state has a high $S=6$ ground state [61], whereas the water-bound $\mathbb{S}_3$ has an $S=3$ ground state [61–65]. Further study of these signals and the conditions that generate them is a continuing and intense research area, and EPR is the frontline technique in this work. Interpretation of the various OEC EPR signals is facilitated by the presence of structurally well-characterized low nuclearity Mn/O model compounds with high ground-state spin, S, values comparable to those found for the OEC.

We recently reported a salt of the cluster cation $[Mn_5O_4(phth)_3(phthH)(bpy)_4]^+$ (**1**; $Mn_2^{IV}Mn_2^{III}Mn^{II}$) [66] that is an extremely rare example of a homo-metallic

cluster in three metal oxidation states, especially at such a low nuclearity. Its $[Mn_5(\mu_3\text{-}O)_2(\mu\text{-}O)_2]^{8+}$ core consists of two near-perpendicular $Mn_3^{II,III,IV}$ scalene triangles fused at the Mn^{II} ion, giving a 'twisted bow tie' topology (Fig. 1). Magnetic susceptibility studies reveal an $S = {}^7/_2$ ground state [66], an unusual situation in mixed-valent Mn/O clusters. This spin value can be rationalized in terms of the classical coupling scheme depicted in Fig. 1b, where the outer dinuclear Mn^{III}/ Mn^{IV} units experience a strong antiferromagnetic coupling such that they may be approximated as possessing a total spin, $S_T^O = {}^1/_2$. Meanwhile, the ferromagnetic (antiferromagnetic) coupling of the Mn^{III} (Mn^{IV}) ions to the central Mn^{II} ensures an overall $S = {}^7/_2$ ground state. Since the Mn nuclearity of **1** and its ground-state S value are both in the ballpark of the OEC and its $\mathbb{S}_n$ states, we decided that it would provide a useful candidate for EPR spectroscopic characterization as a potential reference system for comparison with the OEC $\mathbb{S}_n$ states and other low nuclearity mixed-valence Mn/O complexes, including the handful of $Mn^{IV}/Mn^{III}/$ Mn^{II} complexes analyzed to date by EPR spectroscopy [35, 37, 67–69], most of which are $[Mn_{12}O_{12}(O_2CR)_{16})(H_2O)_4]^{-,2-}$ species. We herein report the results of a high-field EPR (HFEPR) spectroscopic study of **1** and the spin Hamiltonian parameters obtained from spectral simulations. We also attempt to rationalize these parameters based on consideration of the underlying molecular structure of **1**.

Fig. 1 **a** The complete cation of **1** from a viewpoint to emphasize the two near-perpendicular scalene triangles fused at the central Mn^{II} ion, giving rise to a 'twisted bow-tie' topology. Thicker bonds in black denote JT elongation axes and H atoms omitted for clarity. **b** Inter-ion exchange coupling constants deduced from fits to magnetic susceptibility versus temperature data (vs. fit to a Hamiltonian) from Ref. [66]. Also shown are the classical ground-state spin alignments, rationalizing the overall $S = {}^7/_2$ assignment. Color code: Mn^{IV} blue; Mn^{III} green; Mn^{II} violet; O red; N sky blue; C gray (Color figure online)
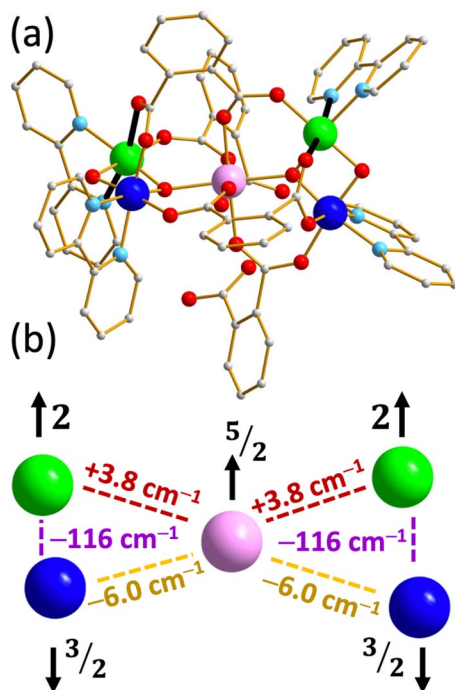
2 Materials and Methods

Complex **1** was prepared according to the procedure described previously [66]. Multi-high-frequency HFEPR measurements were performed on powder samples at the U.S. National High Magnetic Field Laboratory (NHMFL) to quantify the ZFS parameters according to the standard spin Hamiltonian:

$$\widehat{H} = \mu_B \overrightarrow{B} \cdot \widetilde{g} \cdot \widehat{S} + D\widehat{S}_z^2 + E\left(\widehat{S}_x^2 - \widehat{S}_y^2\right), \tag{1}$$

where μ_B is the Bohr magneton, $\overrightarrow{B}$ is the applied magnetic field vector, $\widetilde{g}$ is the Landé tensor, $\widehat{S}$ is the total electronic spin operator with components $\widehat{S}_i$ ($i = x, y, z$), while D and E are the 2nd-order axial and rhombic ZFS parameters, respectively. Spectral simulations were performed using the EasySpin program [70].

HFEPR spectra were recorded on a home-built spectrometer at frequencies of 128 and 256 GHz and temperatures from 8 to 30 K. The transmission-type instrument employs cylindrical light pipes for propagation of microwaves to and from the sample [71]. A wide-band, low-noise, liquid helium cooled (4.2 K) InSb bolometer is used to detect the field modulated signal, dI/dB (I is the transmitted signal intensity and B the applied field). After pre-amplification, the modulated signal is directed to a lock-in amplifier to filter and records the derivative mode (i.e., dI/dB) EPR signal that is in phase with the field modulation. Microwaves are generated using a phase-locked source followed by a multiplier chain (Virginia Diodes, Inc.). A superconducting magnet was used to generate magnetic fields of up to 14.5 T, and temperature control was achieved using a variable-flow helium cryostat (both Oxford Instruments, Plc).

3 Results

Figure 2 displays 8 K powder HFEPR spectra for **1**, recorded at 128 and 256 GHz. Also included in the figure are the best simulations according to Eq. (1). The sharp central resonance, which we believe to be contaminated with an impurity signal, has been removed from the experimental spectra to aid comparison with the simulations (see discussion below and also Fig. 3, where the strong central peak has not been removed). The first thing to note are the positions of the resonances at the extremes of the spectra (labeled x_0 and z_0), as they provide the strongest constraints on the spin Hamiltonian parameters. As can be seen from the temperature dependence of the 256 GHz spectra displayed in Fig. 3, the extreme resonances are cold transitions, i.e., their intensities increase with decreasing temperature, as expected for ground-state excitations corresponding to the principal x, y and z components of the ZFS tensor (see labeling in Figs. 2 and 3). Spectral shifts away from the center of each spectrum, B_c, are due to magnetic anisotropy; $B_c = hf/g\mu_B$, where f is the measurement frequency, h the Planck constant and we assume an isotropic Landé factor, $g_{iso} = 2.00$. As can be seen from Fig. 2,
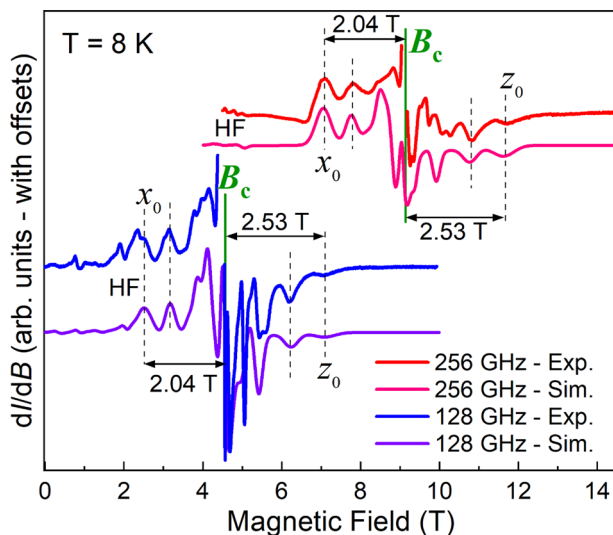
Fig. 2 Experimental spectra (Exp.) and corresponding simulations (Sim.) according to Eq. (1) for frequencies of 128 and 256 GHz (see legend), at a temperature of 8 K. The strong central impurity resonance has been removed from each of the experimental spectra to aid comparison with the simulations (see Fig. 3 and main text for discussion). Resonances marked with vertical dashed lines were used to constrain the simulations, with those at the extremes labeled x_0 and z_0 and their shifts from the center of the spectrum (B_c) indicated. HF marks half-field transitions occurring at $\frac{1}{2}B_c$. Indeed, many higher-order resonances (i.e., $\frac{1}{3}B_c$, $\frac{1}{4}B_c$, etc.) can be seen at low fields in the 128 GHz spectrum on account of the large spin value for **1** and its significant rhombicity

Fig. 3 Temperature dependence of the 256 GHz spectrum (see legend) from which one can infer that the x_0 and z_0 resonances are due to cold transitions because their intensities increase with decreasing temperature (the high-field portion has been expanded to ease viewing). The very strong central resonances display the opposite temperature dependence and are assigned to $m_S = -\frac{1}{2} \rightarrow \frac{1}{2}$ transitions. The sharp peak is attributed to an impurity (see main text), while the shoulder on the high-field edge of this peak is ascribed to **1**, with the blue vertical bars denoting its intensity
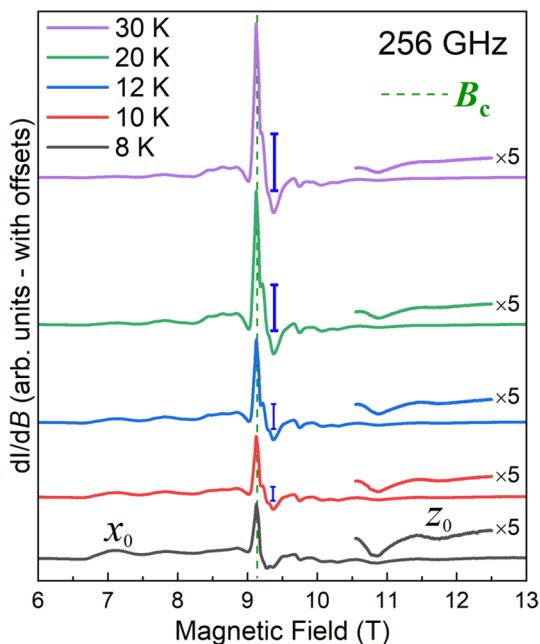
these shifts for the x_0 and z_0 resonances are field- and (frequency-) independent, indicating that the magnetic anisotropy in **1** is dominated by a ZFS interaction. For a uniaxial system ($E=0$), the z_0 and x_0 resonances are expected to shift in a 2:1 ratio relative to B_c (on the basis of Eq. 1): for the easy-axis case ($D<0$), z_0 shifts to the low-field side of B_c by twice the amount of x_0, which appears at the high-field extreme; meanwhile, for the easy-plane case ($D>0$), the spectrum is inverted. As can be seen in Fig. 2, the x_0 and z_0 resonances are almost equidistant from the center of the spectrum, signifying a highly biaxial ZFS tensor, i.e., a significant E parameter. However, the D parameter is clearly positive (easy-plane anisotropy), i.e., the $|B–B_c|$ shift of the extreme resonance on the high-field side of the spectrum ($=2.53$ T) is greater than that on the low-field side ($=2.04$ T)— hence, the highest (lowest) field resonance is labeled z_0 (x_0).

Included in Fig. 2 are the best simulations of the experimental spectra according to Eq. (1), assuming a ground-state spin value, $S=^7/_2$, as deduced from previous fits to magnetic data [66]. As noted in the Introduction, the coupling results in outer $Mn^{III}Mn^{IV}$ $s=^1/_2$ spin vectors that align parallel to that of the central Mn^{II} of $s=^5/_2$, giving a total spin $S=^1/_2+^5/_2+^1/_2=^7/_2$. The EPR simulation strategy involves matching the positions of the outermost x_0 and z_0 peaks, along with their immediate neighbors (see dashed vertical lines in Fig. 2). As noted above, the axial case ($E=0$) enforces a 2:1 ratio on the extreme $|B–B_c|$ shifts. Therefore, the deviation from this ratio uniquely constrains both D and E, provided the $\widetilde{g}$-tensor is known. Given that the cluster is composed of three orbitally non-degenerate ions (Mn^{II} and $2\times Mn^{IV}$) with g-values very close to 2.00, and two Mn^{III} ions with near orthogonal JT axes and $\widetilde{g}$-tensor components that deviate from 2.00 by no more than 2–3%, one would not expect more than 1–2% g-anisotropy for the coupled ground spin state. We therefore assume an isotropic $\widetilde{g}$-tensor, $g_{iso}=2.00$. Although this oversimplifies the physics to some degree, given other unknown factors such as intermolecular interactions (see below), the overall impact of this assumption on the deduced ZFS parameters is expected to be insignificant. Based on this procedure, we determine $D=+0.41(1)$ cm^{-1}, $E=+0.093(6)$ cm^{-1}.

To reproduce the experimental EPR line shapes, we employ a peak-to-peak linewidth of 100 mT along with strains in D and E, $\sigma_D=0.04$ cm^{-1} and $\sigma_E=0.014$ cm^{-1}, respectively. The effect of the strains is to broaden resonances in proportion to how far they are shifted from the center of the spectrum, B_c, as clearly seen in the experiments. Indeed, this is the primary reason why the broad outer resonances have weak intensity in comparison with the sharper features near the center of the spectra. Notably, the central $m_S=–½\rightarrow½$ transitions do not depend on either D or E to first order. This may partially account for the strong intensity right at $B=B_c$, as seen in Fig. 3. However, several factors suggest that that this peak is contaminated by a signal from an impurity. First, the best simulations of the 8 K spectra indicate almost no intensity in the $m_S=–½\rightarrow½$ transitions of **1** (see Fig. 2). This is because the $m_S=–½$ level, which lies $\sim$37 K above ground state at 9 T, should be completely depopulated at 8 K. Nevertheless, the sharp peak seen in Fig. 3 does diminish in intensity at the lowest temperatures. We therefore speculate that it may be due to an excited $m_S=–½\rightarrow½$ transition associated with isolated Mn^{II} or Mn^{IV} impurities, which have lower total spin values compared to **1** and, thus, their

$m_S = -\frac{1}{2}$ levels will remain appreciably populated even at 8 K. A second factor is the shape of this resonance, i.e., it emerges as a peak rather than a derivative shape, suggesting saturation effects, which are known to cause this type of line shape anomaly. Again, this is indicative of an isotropic species displaying slow spin–lattice relaxation, i.e., Mn^{II} or Mn^{IV}. Instead, the excited $m_S = -\frac{1}{2} \rightarrow \frac{1}{2}$ transitions associated with **1** most likely correspond to the narrow shoulder on the high-field side of the sharp resonance, suggesting an actual g-value slightly below 2.00 (~ 1.99). As expected, this feature can be seen to increase in amplitude with increasing temperature (see vertical blue bars in Fig. 3).

4 Discussion

The obtained positive sign of D is consistent with the preceding discussion. Indeed, it is impossible to achieve good simulations with other spin values or with a negative D parameter, subject to the constraint $E/D \leq \frac{1}{3}$ [70]. Meanwhile, the actual E/D ratio of 0.227 is close to the maximal biaxial limit of $\frac{1}{3}$. This begs the question as to the reasons for these observations. The Mn^{III} centers represent the main source of single-ion anisotropy, yet the isolated JT elongated species possess easy-axis anisotropy ($d < 0$, lowercase is used here to differentiate between single-ion and molecular ZFS parameters). However, the situation in exchange-coupled clusters is not so straightforward. Indeed, one may obtain either sign of D, or even zero overall 2nd-order anisotropy in some special topologies [72]. To illustrate this point, we consider two easy-axis Mn^{III} ions (see Fig. 4). If their easy-axes are parallel, then the coupled system will also possess an easy- (z-) axis anisotropy ($D < 0$). However, if the easy-axes are perpendicular, then the spin associated with the coupled system will prefer to orient within the plane containing the two easy-axes (see insert to Fig. 4b), i.e., it will possess an easy-plane ($D > 0$) with a hard (z-) axis perpendicular to this plane. In these two extreme cases (parallel/perpendicular), the E parameter is exactly zero (assuming the single-ion ZFS tensors are cylindrically symmetric, i.e., $e = 0$). In the parallel case, the coupled ZFS tensor would inherit the cylindrical symmetry of the single-ion tensors, i.e., $E = 0$, and the axial parameter can be calculated using matrix projection techniques, giving $D = D_0 = \frac{3}{7}d$ [72–75]. In the perpendicular case, the coupled ZFS tensor acquires a tetragonal symmetry, for which E is also strictly zero; in this case, the fourfold anisotropy within the easy-plane due to the orthogonal easy-axes of the Mn^{III} ions emerges only at the fourth order in spin operators, i.e., through $\hat{O}_4^4 \left[= \frac{1}{2}\left(\hat{S}_x^4 + \hat{S}_y^4\right)\right]$; the strengths of such interactions are known to diminish with increasing exchange coupling within the molecule [72, 76, 77]. For all cases in between ($\theta \neq 0$ or $90°$, where θ is the angle between easy-axes), a rhombic anisotropy emerges, i.e., a finite E value, with the sign of both D and E switching at the maximally rhombic point when $E/D = \frac{1}{3}$.

To reinforce the above qualitative discussion, we performed an exact mapping between a two-spin model and Eq. (1). Our eventual aim here is to rationalize the easy-plane anisotropy obtained for **1**. For the sake of simplicity (see below), we consider two axially symmetric $S = 2$ spins (representing Mn^{III} ions with $e = 0$ and
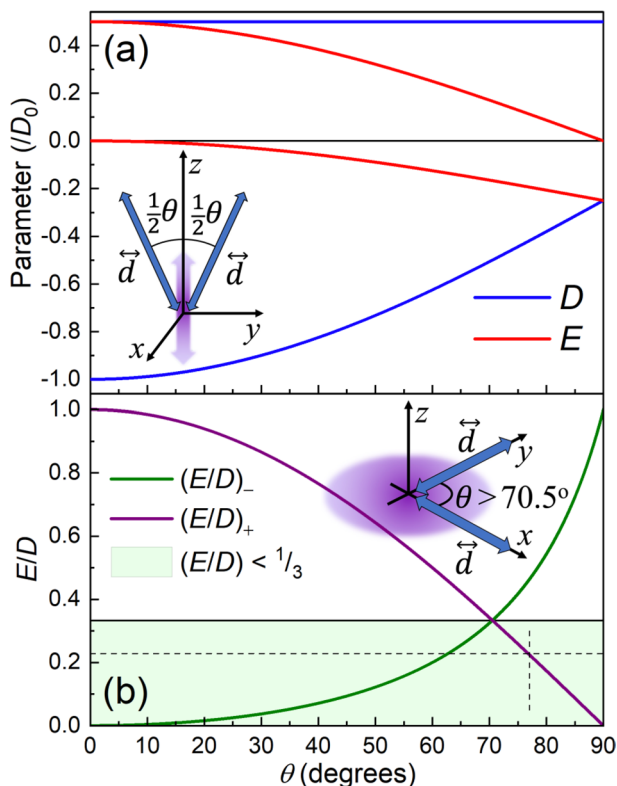
Fig. 4 Mapping between the two-spin model and Eq. (1) [see main text for details]: **a** the obtained D and E parameterizations and **b** the associated $(E/D)_-$ and $(E/D)_+$ ratios. Insets depict the orientations of the local tensors relative to the coordinate frames of the molecular ZFS tensors for the easy-axis (**a**) and easy-plane (**b**) situations, along with the preferred spin orientations in the two cases (purple shading). The functional forms of the curves for the interval are as follows: $D_- = -\frac{1}{2}D_0\{3\cos^2(\theta/2) - 1\}$; $E_- = -\frac{1}{4}D_0(1 - \cos\theta)$; $D_+ = +\frac{1}{2}D_0$; $E_+ = +\frac{1}{2}D_0\cos\theta$; $(E/D)_- = \frac{1}{2}(1 - \cos\theta)/\{3\cos^2(\theta/2) - 1\}$; and $(E/D)_+ = \cos\theta$

identical d parameters) with their local easy-axes separated by an angle θ (see insets to Fig. 4). We then introduce a strong ferromagnetic Heisenberg exchange between the $S = 2$ spins such that the coupling, J (~ 3300 cm^{-1}), is substantially stronger than all other interactions, thus avoiding complications due to emergent 4th- and higher-order ZFS terms in Eq. (1). We also assume $g_{\mathrm{iso}} = 2.00$ for the $S = 2$ spins. Figure 4 displays the results of this mapping onto a total $S = 4$ state according to Eq. (1); mathematical expressions for each curve are given in the figure caption.

As can be seen in Fig. 4(a), two parameterizations are obtained for each value of θ, one with positive D and E, and the other with negative values. [N.B. there are actually four parameterizations, as the sign of E is indeterminate; however, the accepted convention is for E/D to be positive.] Though often overlooked in the molecular magnetism community, this is a well-known property of the effective spin Hamiltonian formalism [70, 78]. At the extremes, the mapping reaffirms

the anticipated results, namely that parallel easy-axes ($\theta = 0$) yield a negative D parameter ($= -D_0$), while the perpendicular case ($\theta = 90^\circ$) yields a positive $D = \frac{1}{2}D_0$, with $E = 0$ in both cases. However, in either situation, there is another parameterization with opposite sign of D and finite $E = D$ ($= +\frac{1}{2}D_0$ at $\theta = 0$ and $-\frac{1}{4}D_0$ at $\theta = 90^\circ$). Although these solutions do in fact possess cylindrical symmetry, they are counterintuitive because of the finite rhombic parameter and the symmetry axis is not along z. For this reason, the accepted convention is to adopt the $E = 0$ parameterizations, with the principal symmetry axis defined by z according to Eq. (1). In between these limits, the system acquires orthorhombic (D_{2h}) symmetry.

Figure 4b plots E/D for the negative and positive ZFS parameterizations [$(E/D)_-$ and $(E/D)_+$, respectively], which uniquely characterizes the degree of (ortho)rhombicity. As can be seen, the curves cross at $\theta_c = 70.5^\circ$, where $E/D = \frac{1}{3}$. Therefore, the accepted convention is to adopt only the parameterization for which $E/D \leq \frac{1}{3}$ [70]. Most notably, the principal symmetry (z-) axis of Eq. (1) undergoes a rotation relative to the molecular frame at θ_c (see Fig. 4 insets): for $\theta < \theta_c$, it lies in the same plane as the local ZFS tensors of the two Mn^{III} ions; for $\theta > \theta_c$, it lies perpendicular to this plane. Right at $\theta = \theta_c$, one can equally describe the ZFS tensor as having an easy-axis with a perpendicular plane containing hard and medium directions ($D < 0$), or a hard axis with a perpendicular plane containing easy and medium directions ($D > 0$). It is important to stress that there is no dramatic change in the spin physics at $\theta = \theta_c$. The preferred spin orientation lies within the plane containing the two $\vec{d}$-tensors in both cases: for $\theta \ll \theta_c$, the preferred (z-) orientation dissects the local $\vec{d}$-tensor axes (inset to Fig. 4a); for $\theta > \theta_c$, the preferred orientations are delocalized within the (xy-) plane containing the two tensors (inset to Fig. 4b). All that changes are the coordinate frames and the way that the anisotropy is described, i.e., easy-axis ($\theta < \theta_c$) and easy-plane ($\theta > \theta_c$).

At this juncture, we take a step back to ask whether the simple mapping in Fig. 4 can teach us anything about the Mn_5 molecule. First, as with many related clusters [79], we anticipate that the magnetic anisotropy associated with the $S = \frac{7}{2}$ ground state derives primarily from the two JT elongated octahedral Mn^{III} ions, because their near-orbital degeneracy gives rise to ZFS interactions that are typically at least an order-of-magnitude stronger than those of Mn^{II} or Mn^{IV}. Likewise, one can estimate that the summed spin–spin dipolar contributions are minimal; the worst (hypothetical) case, with all spins in a line, would contribute less than 1/10th of the observed anisotropy energy scale. One may then ask how the strongly coupled effective $S = \frac{1}{2}$ Mn^{III}/Mn^{IV} units can relay the Mn^{III} anisotropy to the more weakly coupled $S = \frac{7}{2}$ state. Provided that the ground state is reasonably isolated from excited states (i.e., that the total $S = \frac{7}{2}$ spin is a good quantum number), then it is well established that the projected cluster anisotropy depends only on the coupling scheme and not on the strengths of the individual coupling interactions [73, 75]. One may rationalize this is in terms of the emergence of an anisotropic exchange coupling within the effective model that treats the peripheral Mn^{III}/Mn^{IV} units as $S = \frac{1}{2}$ spins; of course, these anisotropic exchange interactions arise through higher-order processes involving the excited spin states of the coupled Mn^{III}/Mn^{IV} units [80], so the Mn^{III} anisotropy is never really lost.

For the aforementioned reasons, we believe that the two-spin model described in Fig. 4 can teach us a great deal about compound **1**. The addition of the three isotropic ions ($2 \times Mn^{IV} + Mn^{II}$) simply renormalizes the absolute values of the molecular D and E parameters, but it should not alter the geometrical considerations. If one makes the assumption that the local ZFS tensors of the Mn^{III} ions are aligned with their JT axes, the orientations of which we determine from the average of the elongated Mn–O and Mn–N contacts (dark bonds in Fig. 1), one can then estimate a value of $\theta = 78°$ for **1**. Meanwhile, on the basis of the spectral simulations in Fig. 2, the ortho-rhombicity, $(E/D)_+ = 0.227$. This gives remarkably good agreement with the two-spin model, which predicts $\theta = \cos^{-1}(E/D) = 77°$ (see dashed lines in Fig. 4b). The near-perfect agreement may be somewhat fortuitous, given that our model neglects any local rhombic contributions to the Mn^{III} anisotropy (i.e., $e = 0$) and the simplifying assumption about the orientations of the $\bar{d}$-tensors along the O–Mn–N contacts. Nevertheless, there is a little doubt that the spirit of this model allows us to rationalize the positive D parameter for **1** on account of the near-perpendicular disposition of the Mn^{III} JT distortions, and the significant bi-axiality of its 2nd-order ZFS tensor because of the very strong variation of E in the vicinity of $\theta = 90°$ (Fig. 4), i.e., just a 10–15° deviation from 90° can give rise to extreme bi-axiality. Predicting the magnitudes of the molecular D and E parameters of the Mn_5 molecule is less straightforward, given the complicated coupling scheme [75]. A very rough estimate may be obtained from the coupled $S = 4$ state of two Mn^{III} ions, which differs in total spin by a single unpaired electron. In this case, $D_0 = \frac{3}{7}d$, and the positive parameterization gives $D = \frac{1}{2}|D_0| = \frac{3}{14}|d|$ [73], where d is the single-ion ZFS parameter. If one assumes $d \approx - 4\,cm^{-1}$, this gives a D parameter that is within a factor of two of the experimental one. However, it should be stressed that this represents a rather crude estimate.

In spite of the good agreement found for the resonance positions marked by the vertical dashed lines in Fig. 2, additional fine structures and peak splittings associated with sharper resonances closer to the center of the spectrum are not well captured by the simulations, especially for the lower-frequency measurement. This could be due to population of excited spin states or intermolecular interactions. Capturing either of these effects in the simulations is challenging, requiring considerable computational resources: the former requires adoption of a multi-spin Hamiltonian, which would be highly over-parameterized for such a low-symmetry molecule with five metal centers [matrix dimension $(5^2 \times 4^2 \times 6)^2 = 2400 \times 2400$]; the latter would require a model coupling multiple $S = {}^7/_2$ molecules [matrix dimension 64×64 for a dimer and much larger for a more realistic description]. We suspect that the additional fine structures are due mainly to intermolecular interactions mediated by the close π–π contacts associated with the $phth^{2-}$ ligands, as well as weaker bpy–bpy contacts between neighboring Mn_5 cations (see Fig. 5).

Finally, we comment on the agreement between the present investigation and the original magnetic measurements reported in Ref. [66]. EPR measurements cannot inform on the magnitudes of the pairwise interactions depicted in Fig. 1b. However, the spectra are quite consistent with the $S = {}^7/_2$ ground-state spin value, suggesting that the coupling scheme determined from the magnetic fits is the correct one. By contrast, the Ref. [66] reported a negative ZFS interaction, with
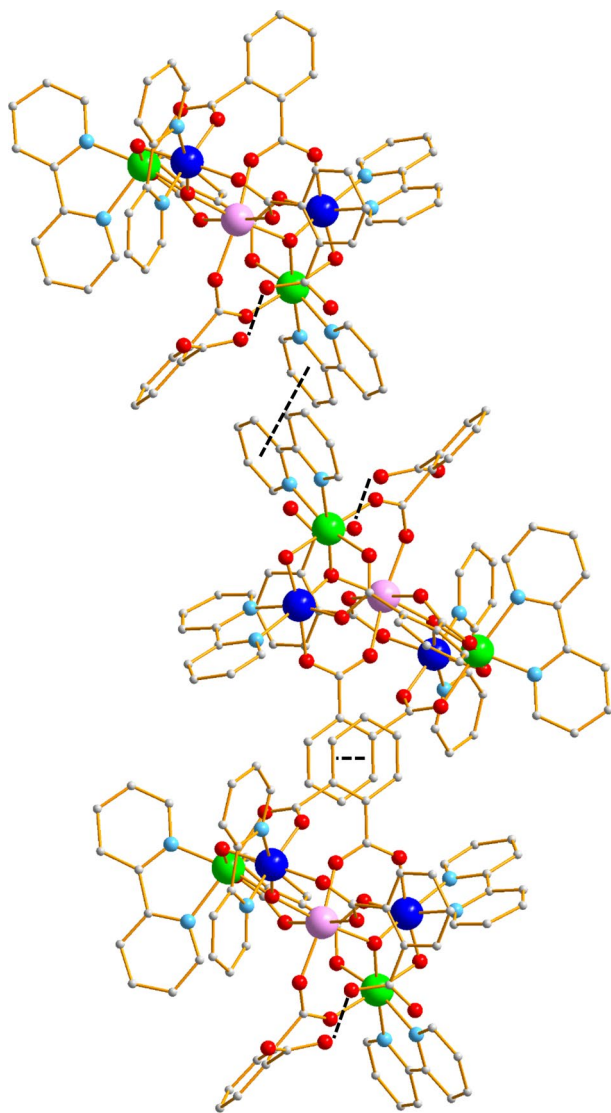
Fig. 5 Extended view of the crystal structure of **1** highlighting several close intermolecular contacts (dashed black lines). Of particular relevance to this investigation are the close π–π contacts associated with the phth²⁻ ligands and the weaker bpy–bpy contacts. Color code: Mn^{IV} blue; Mn^{III} green; Mn^{II} violet; O red; N sky blue; C gray (Color figure online)

$D = -0.36$ cm^{-1}, in contrast to the value reported here. However, this is a well-known problem in fits to magnetization data, which always give minima for both positive and negative D parameters, i.e., such fits are not particularly sensitive to the sign of D, particularly in highly rhombic cases. Interestingly, the fits in Ref. [66] give a second minimum in the error surface (plotted versus g and D)

with a positive D value and a root-mean-square error that is only marginally inferior (50% larger) than that of the negative parameterization. The corresponding axial ZFS parameter, $D_+ = +0.51 \text{ cm}^{-1}$, with $g \approx 2.0$, is fully consistent with the present investigation. This demonstrates that the signs of D parameters obtained from such fits should be taken at face value, something that is often underappreciated in the molecular magnetism community. EPR is really needed to determine both the signs and accurate values of ZFS tensor components.

5 Conclusions

We report a detailed HFEPR investigation of an unusual mixed-valent $Mn_2^{IV}Mn_2^{III}Mn^{II}$ cluster and carry out a detailed analysis and modeling of its magnetic properties. The molecule possesses a highly biaxial ZFS tensor ($E/D = 0.227$) with overall easy-plane anisotropy ($D > 0$), in spite of the fact that the main contributors to this anisotropy are the two Mn^{III} ions that possess easy-axis ($d < 0$) ZFS tensors. We develop a microscopic model which relates the sign of D and the degree of ortho-rhombicity, E/D, to the underlying structure of the molecule. In particular, the angle between the JT axes on the Mn^{III} ions is shown to uniquely dictate the overall magnetic behavior. This study illustrates the tremendous power of HFEPR for extracting detailed structural information concerning polynuclear manganese clusters such as **1**. These findings may prove relevant to many related molecules that are of interest because of their catalytic properties, including the ability to oxidize water and evolve oxygen. Most EPR studies of such systems are performed at low fields, with high g-factor signals used to inform on the overall spin states of the clusters. By contrast, we show here how HFEPR provides access to the molecular ZFS interactions which, in turn, yield unique structural fingerprints of the Mn^{III} coordination environments.

Declarations

References

1. J.E. Post, Proc. Natl. Acad. Sci. USA **96**, 3447 (1999)
2. R. Jacob, S. Raman Sankaranarayanan, S.P. Kumaresh Babu, Mater. Today Proc. **27**, 2852 (2019)
3. M.A. Islam, D.W. Morton, B.B. Johnson, B. Mainali, M.J. Angove, J. Water Process Eng. **26**, 264 (2018)
4. Y. Umena, K. Kawakami, J.R. Shen, N. Kamiya, Nature **473**, 55 (2011)
5. N. Kamiya, J.R. Shen, Proc. Natl. Acad. Sci. USA **100**, 98 (2003)
6. K.N. Ferreira, T.M. Iverson, K. Maghlaoui, J. Barber, S. Iwata, Science **303**, 1831 (2004)
7. J. Barber, J.W. Murray, Coord. Chem. Rev. **252**, 233 (2008)
8. H. Dau, A. Grundmeier, P. Loja, M. Haumann, Philos. Trans. R. Soc. B Biol. Sci. **363**, 1237 (2008)
9. P.E.M. Siegbahn, Chem. A Eur. J. **14**, 8290 (2008)
10. A. Guskov, J. Kern, A. Gabdulkhakov, M. Broser, A. Zouni, W. Saenger, Nat. Struct. Mol. Biol. **16**, 334 (2009)
11. L. Fan, Z. Tu, S.H. Chan, Energy Rep. **7**, 8421 (2021)
12. M.K. Singla, P. Nijhawan, A.S. Oberoi, Environ. Sci. Pollut. Res. **28**, 15607 (2021)
13. I. Staffell, D. Scamman, A. Velazquez Abad, P. Balcombe, P.E. Dodds, P. Ekins, N. Shah, K.R. Ward, Energy Environ. Sci. **12**, 463 (2019)
14. M. Yue, H. Lambert, E. Pahon, R. Roche, S. Jemei, D. Hissel, Renew. Sustain. Energy Rev. **146**, 111180 (2021)
15. J.S. Kanady, E.Y. Tsui, M.W. Day, T. Agapie, Science **333**, 733 (2013)
16. H.B. Lee, A.A. Shiau, D.A. Marchiori, P.H. Oyala, B. Yoo, J.T. Kaiser, D.C. Rees, R.D. Britt, T. Agapie, Angew. Chemie Int. Ed. **60**, 17671 (2021)
17. S. Mukherjee, J.A. Stull, J. Yano, T.C. Stamatatos, K. Pringouri, T.A. Stich, K.A. Abboud, R.D. Britt, V.K. Yachandra, G. Christou, Proc. Natl. Acad. Sci. USA **109**, 2257 (2012)
18. C. Zhang, C. Chen, H. Dong, J.-R. Shen, H. Dau, J. Zhao, Science **348**, 690 (2015)
19. I.J. Hewitt, J.K. Tang, N.T. Madhu, R. Clérac, G. Buth, C.E. Anson, A.K. Powell, Chem. Commun. **9**, 2650 (2006)
20. L.B. Jerzykiewicz, J. Utko, M. Duczmal, P. Sobota, Dalt. Trans. **8**, 825 (2007)
21. V. Kotzabasaki, M. Siczek, T. Lis, C.J. Milios, Inorg. Chem. Commun. **14**, 213 (2011)
22. A. Mishra, W. Wernsdorfer, K.A. Abboud, G. Christou, Chem. Commun. **1**, 54 (2005)
23. A.A. Alaimo, E.S. Koumousi, L. Cunha-Silva, L.J. Mccormick, S.J. Teat, V. Psycharis, C.P. Rapto-poulou, S. Mukherjee, C. Li, S. Das Gupta, A. Escuer, G. Christou, T.C. Stamatatos, Inorg. Chem. **56**, 10760 (2017)
24. H.B. Lee, D.A. Marchiori, R. Chatterjee, P.H. Oyala, J. Yano, R.D. Britt, T. Agapie, J. Am. Chem. Soc. **142**, 3753 (2020)
25. J.S. Kanady, P. Lin, K.M. Carsch, R.J. Nielsen, M.K. Takase, W.A. Goddard, T. Agapie, J. Am. Chem. Soc. **136**, 14374 (2014)
26. E.Y. Tsui, T. Agapie, Proc. Natl. Acad. Sci. USA **110**, 10084 (2013)
27. A.M. Ako, C.E. Anson, R. Clérac, A.J. Fitzpatrick, H. Müller-Bunz, A.B. Carter, G.G. Morgan, A.K. Powell, Polyhedron **206**, 115325 (2021)
28. R. Yao, Y. Li, Y. Chen, B. Xu, C. Chen, C. Zhang, J. Am. Chem. Soc. **143**, 17360 (2021)
29. Y. Mousazade, M.R. Mohammadi, R. Bagheri, R. Bikas, P. Chernev, Z. Song, T. Lis, M. Siczek, N. Noshiranzadeh, S. Mebs, H. Dau, I. Zaharieva, M.M. Najafpour, Dalt. Trans. **49**, 5597 (2020)
30. S. Tandon, J. Soriano-López, A.C. Kathalikkattil, G. Jin, P. Wix, M. Venkatesan, R. Lundy, M.A. Morris, G.W. Watson, W. Schmitt, Sustain. Energy Fuels **4**, 4464 (2020)
31. Z. Han, K.T. Horak, H.B. Lee, T. Agapie, J. Am. Chem. Soc. **139**, 9108 (2017)
32. G. Maayan, N. Gluz, G. Christou, Nat. Catal. **1**, 48 (2018)
33. M.L. Baker, S.J. Blundell, N. Domingo, S. Hill, In molecular nanomagnets. Struct. Bond. **164**, 231–292 (2015)
34. S. Hill, Polyhedron **64**, 128–135 (2013)
35. C. Lampropoulos, C. Koo, S.O. Hill, K. Abboud, G. Christou, Inorg. Chem. **47**, 11180 (2008)
36. R. Gupta, T. Taguchi, B. Lassalle-Kaiser, E.L. Bominaar, J. Yano, M.P. Hendrich, A.S. Borovik, Proc. Natl. Acad. Sci. USA **112**, 5319 (2015)
37. M. Murugesu, S. Takahashi, A. Wilson, K.A. Abboud, W. Wernsdorfer, S. Hill, G. Christou, Inorg. Chem. **47**, 9459 (2008)

38. S. Das Gupta, R.L. Stewart, D.T. Chen, K.A. Abboud, H.P. Cheng, S. Hill, G. Christou, Inorg. Chem. **59**, 8716 (2020)
39. T.N. Nguyen, W. Wernsdorfer, M. Shiddiq, K.A. Abboud, S. Hill, G. Christou, Chem. Sci. **7**, 1156 (2016)
40. S. Hill, N. Anderson, A. Wilson, S. Takahashi, N.E. Chakov, M. Murugesu, J.M. North, N.S. Dalal, G. Christou, J. Appl. Phys. **97**, 10 (2005)
41. T. Ghosh, J. Marbey, W. Wernsdorfer, S. Hill, K.A. Abboud, G. Christou, Phys. Chem. Chem. Phys. **23**, 8854 (2021)
42. T.N. Nguyen, M. Shiddiq, T. Ghosh, K.A. Abboud, S. Hill, G. Christou, J. Am. Chem. Soc. **137**, 7160 (2015)
43. N. Aliaga-Alcalde, R.S. Edwards, S.O. Hill, W. Wernsdorfer, K. Folting, G. Christou, V. Gaines, L.L. Ne, A.V. Martyrs, J. Am. Chem. Soc. **3**, 12503 (2004)
44. K.M. Poole, M. Korabik, M. Shiddiq, K.J. Mitchell, A. Fournet, Z. You, G. Christou, S. Hill, M. Hołyńska, Inorg. Chem. **54**, 1883 (2015)
45. M. Shiddiq, D. Komijani, Y. Duan, A. Gaita-Ariño, E. Coronado, S. Hill, Nature **531**, 348 (2016)
46. K. Kundu, J.R.K. White, S.A. Moehring, J.M. Yu, J.W. Ziller, F. Furche, W.J. Evans, S. Hill, Nat. Chem. **14**, 392 (2022)
47. T.A. Stich, S. Lahiri, G. Yeagle, M. Dicus, M. Brynda, A. Gunn, C. Aznar, V.J. DeRose, R.D. Britt, Appl. Magn. Reson. **31**, 321 (2007)
48. C.H. Chang, D. Svedružić, A. Ozarowski, L. Walker, G. Yeagle, R.D. Britt, A. Angerhofer, N.G.J. Richards, J. Biol. Chem. **279**, 52840 (2004)
49. S.K. Smoukov, J. Telser, B.A. Bernat, C.L. Rife, R.N. Armstrong, B.M. Hoffman, J. Am. Chem. Soc. **124**, 2318 (2002)
50. I.D. Sahu, R.M. McCarrick, G.A. Lorigan, Biochemistry **52**, 5967 (2013)
51. V. Krewald, M. Retegan, F. Neese, W. Lubitz, D.A. Pantazis, N. Cox, Inorg. Chem. **55**, 488 (2016)
52. M. Drosou, G. Zahariou, D.A. Pantazis, Angew. Chem. Int. Ed. **60**, 13943 (2021)
53. Z. Sun, D. Ruiz, N. R. Dilley, M. Soler, J. Ribas, K. Folting, M. B. Maple, G. Christou, and D. N. Hendrickson, Chem. Commun. **19**, 1973 (1999)
54. M. Soler, W. Wernsdorfer, Z. Sun, J.C. Huffman, D.N. Hendrickson, G. Christou, Chem. Commun. **12**, 2672 (2003)
55. N.E. Chakov, S.C. Lee, A.G. Harter, P.L. Kuhns, A.P. Reyes, S.O. Hill, N.S. Dalal, W. Wernsdorfer, K.A. Abboud, G. Christou, J. Am. Chem. Soc. **128**, 6975 (2006)
56. G.C. Dismukes, Y. Siderer, Proc. Natl. Acad. Sci. **78**, 274 (1981)
57. J.L. Zimmermann, A.W. Rutherford, Biochemistry **25**, 4609 (1986)
58. A. Haddy, K.V. Lakshmi, G.W. Brudvig, H.A. Frank, Biophys. J. **87**, 2885 (2004)
59. A. Haddy, Photosynth. Res. **92**, 357 (2007)
60. D.A. Pantazis, W. Ames, N. Cox, W. Lubitz, F. Neese, Angew. Chem. Int. Ed. **51**, 9935 (2012)
61. G. Zahariou, N. Ioannidis, Y. Sanakis, D.A. Pantazis, Angew. Chem. Int. Ed. **60**, 3156 (2021)
62. A. Boussac, M. Sugiura, A.W. Rutherford, P. Dorlet, J. Am. Chem. Soc. **131**, 5050 (2009)
63. A. Boussac, A.W. Rutherford, M. Sugiura, Biochim. Biophys. Acta Bioenerg. **1847**, 576 (2015)
64. N. Cox, M. Retegan, F. Neese, D.A. Pantazis, A. Boussac, W. Lubitz, Science **345**, 804 (2014)
65. D.A. Marchiori, R.J. Debus, R.D. Britt, Biochemistry **59**, 4864 (2020)
66. A.R. Hale, P. King, K.A. Abboud, G. Christou, Polyhedron **200**, 115141 (2021)
67. C. Pastor-Ramírez, R. Ulloa, D. Ramírez-Rosales, H. Vázquez-Lima, S. Hernández-Anzaldo, Y. Reyes-Ortega, Crystals **8**, 447 (2018)
68. R. Bagai, G. Christou, Chem. Soc. Rev. **38**, 1011 (2009)
69. M. Soler, P. Mahalay, W. Wernsdorfer, D. Lubert-Perquel, J.C. Huffman, K.A. Abboud, S. Hill, G. Christou, Polyhedron **195**, 114968 (2021)
70. S. Stoll, A. Schweiger, J. Magn. Reson. **178**, 42 (2006)
71. A.K. Hassan, L.A. Pardi, J. Krzystek, A. Sienkiewicz, P. Goy, M. Rohrer, L.-C. Brunel, J. Magn. Reson. **142**, 300–312 (2000)
72. J. Marbey, P.-R. Gan, E.-C. Yang, S. Hill, Phys. Rev. B **98**, 144433 (2018)
73. A. Bencini, D. Gatteschi, *EPR of exchange coupled systems* (Springer-Verlag, New York, 1990)
74. S. Hill, S. Datta, J. Liu, R. Inglis, C.J. Milios, P.L. Feng, J.J. Henderson, E. del Barco, E.K. Brechin, D.N. Hendrickson, Dalton Trans. Chem. **39**, 4693 (2010)
75. S. Datta, E. Bolin, R. Inglis, C.J. Milios, E.K. Brechin, S. Hill, Polyhedron **28**, 1911 (2009)
76. A. Wilson, J. Lawrence, E.-C. Yang, M. Nakano, D.N. Hendrickson, S. Hill, Phys. Rev. B **74**, 140403(R) (2006)

77. J. Liu, E. del Barco, S. Hill, Phys. Rev. B **85**, 012406 (2012)
78. X. Feng, J. Liu, T.D. Harris, S. Hill, J.R. Long, J. Am. Chem. Soc. **134**, 7521 (2012)
79. E. del Barco, S. Hill, C.C. Beedle, D.N. Hendrickson, I.S. Tupitsyn, P.C.E. Stamp, Phys. Rev. B **82**, 104426 (2010)
80. S.M. Winter, S. Hill, R.T. Oakley, J. Am. Chem. Soc. **137**, 3720 (2015)